Quantum dynamics of an atomic double-well system interacting with a trapped ion

Joger, J.; Negretti, A.; Gerritsma, R.

DOI
10.1103/PhysRevA.89.063621

Publication date
2014

Document Version
Final published version

Published in
Physical Review A - Atomic, Molecular, and Optical Physics

Quantum dynamics of an atomic double-well system interacting with a trapped ion

J. Joger,[1] A. Negretti,[2] and R. Gerritsma[1,*]

[1]*Institut für Physik, Johannes Gutenberg-Universität Mainz, D-55099 Mainz, Germany*

[2]*Zentrum für Optische Quantentechnologien and The Hamburg Centre for Ultrafast Imaging, Universität Hamburg, Luruper Chaussee 149, D-22761 Hamburg, Germany*

(Received 4 April 2014; published 25 June 2014)

We analyze theoretically the dynamics of an atomic double-well system with a single ion trapped in its center. We find that the atomic tunneling rate between the wells depends both on the spin of the ion via the short-range spin-dependent atom-ion scattering length and on its motional state with tunneling rates reaching hundreds of hertz. A protocol is presented that could transport an atom from one well to the other, depending on the motional (Fock) state of the ion within a few milliseconds. This phonon-atom coupling is of interest for creating atom-ion entangled states and may form a building block in constructing a hybrid atom-ion quantum simulator. We also analyze the effect of imperfect ground-state cooling of the ion and the role of micromotion when the ion is trapped in a Paul trap. Due to the strong nonlinearities in the atom-ion interaction, the micromotion can cause couplings to high-energy atom-ion scattering states, preventing accurate state preparation and complicating the double-well dynamics. We conclude that the effects of micromotion can be reduced by choosing ion-atom combinations with a large mass ratio and by choosing large interwell distances. The proposed double-well system may be realized in an experiment by combining either optical traps or magnetic microtraps for atoms with ion trapping technology.

DOI: 10.1103/PhysRevA.89.063621 PACS number(s): 03.75.Gg, 03.75.Lm, 37.10.Ty, 34.50.Cx

I. INTRODUCTION

Recent experiments involving a combination of ultracold quantum gases and trapped ions have sparked significant interest in studying their properties in the quantum regime [1–5]. These experiments explore sympathetic cooling of ions by means of clouds of cold atoms [6] and study cold chemistry [7]. Trapped single ions may be used to perform *in situ* measurements of cold atomic gases in lattice potentials [8] or to study the physics of impurities in one-dimensional Bose gases [9]. The excellent controllability of trapped ions together with the near-perfect state preparation and readout may also allow experiments in which ions *control* the dynamics of ultracold atoms. For instance, it has been proposed that an entangling quantum gate operation could be performed on a single trapped atom and ion by means of a controlled collision [10]. Here the spin dependence of the scattering cross section can be used to obtain a state-dependent collisional phase shift, leading to the desired quantum logic [11,12]. In a recent paper we showed that a similar controllability should arise when a single trapped ion is placed in between a double-well atomic Josephson junction. Here the spin of the ion would control the tunneling rate of atoms between the wells via the state-dependent short-range interactions of the atoms and ion [13]. Since the ion could in this way control many-body dynamics, mesoscopic entanglement between the atomic matter wave and the spin of the ion may be created. The interplay between the spin-dependent tunneling and the interatomic interactions could also result in superpositions of quantum self-trapping [14] and Josephson tunneling. Since trapped ions allow for superb experimental control, they may be better suited to investigate Josephson physics than using single atomic impurities [15,16].

Including a single trapped ion expands on the rich dynamics of the Josephson junction as described in numerous experimental and theoretical works [14,17–25]. Furthermore, the system may be seen as a unit cell for a larger-scale hybrid atom-ion quantum simulator [26]. Constructing such a device by concatenating ion-controlled double wells could be a natural way to combine quantum simulators in which atoms can tunnel between sites in an optical lattice [27] with simulators employing the pseudospin and collective motional states of ion crystals [28]. In such a system, atomic Bloch waves would interact with phononic excitations in the ion crystal, leading to solid-state phenomena such as Peierls instabilities [26,29] and phonon-mediated interactions. In particular, such a hybrid system may enable the investigation of superconductivity in a more natural way, where fermionic atoms would play the role of electrons in a solid-state system, than atoms trapped in optical lattices, where the backaction of the atoms on the lattice is more difficult to reproduce.

In Ref. [13] we solved the atomic dynamics in the ion-controlled double-well system by assuming that the ion is pinned to the center of its trap. In this work we investigate how the dynamics of the ion changes the picture obtained in Ref. [13]. To this end, we consider a setup in which an atom is trapped in a double-well potential with a single ion trapped in its center as shown in Fig. 1. We will numerically solve the combined atom-ion dynamics in one dimension in terms of quantum-defect theory (QDT) [30,31]. This enables us to investigate the possibility of using nonclassical states of the ion motion to control the tunneling and the effect of imperfect ground-state cooling on the dynamics. We also address the role of micromotion—the fast oscillating motion of ions caused by a time-dependent Paul trap—on the tunneling dynamics. This effect has been shown to significantly change the dynamics of the proposed atom-ion quantum gate [10], as described in Ref. [32], leading to slower gates or requiring additional control pulses. Micromotion has also been shown to limit attainable temperatures for ions that are sympathetically

*rene.gerritsma@uni-mainz.de; http://www.hyqs.uni-mainz.de.

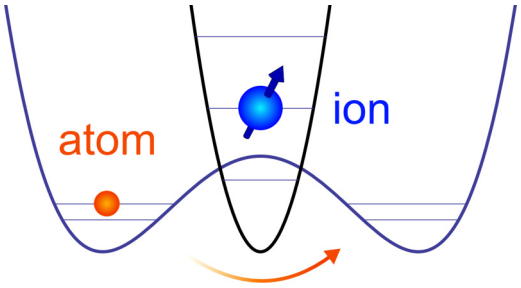

FIG. 1. (Color online) We consider a setup in which an atom is trapped in a double-well potential with a single ion trapped in its center. The quantized motional states of the ion and its internal spin state influence the atomic tunneling rate between the wells. These degrees of freedom can in turn be manipulated with laser light or radio-frequency fields.

cooled by atoms [33,34]. Here we show that the micromotion causes difficulties in state preparation and complicates the atomic tunneling for large tunneling rates, i.e., small interwell separations. Additionally, we find that using an atom-ion combination with a large mass ratio, with the ion being the heavier particle, allows one to overcome such difficulties. This conclusion is in line with a recent classical analysis studying attainable temperatures in atom-ion sympathetic cooling [33].

The paper is structured as follows. In Sec. II we discuss the solutions to the atomic double well in the presence of a static ion. In Sec. III we calculate how the situation changes when the ion dynamics are taken into account. We show that the motional state of the ion is coupled to the atomic tunneling rate such that the tunneling can be controlled by engineering (nonclassical) ionic states of motion. We also analyze the effect of imperfect ion cooling. In Sec. IV we analyze the problem in the presence of a time-dependent trapping potential for the ion and the effect of micromotion. We discuss possible experimental implementations in Sec. V and summarize in Sec. VI. In Appendix A we solve the double-well problem in three dimensions and demonstrate that the one-dimensional calculation results in the same physical picture. Finally, in Appendix B we provide some details on the derivation of the micromotion Hamiltonian.

II. A STATIC ION IN ONE DIMENSION

The interaction between an atom and an ion is caused by an induced atomic dipole due to the electric field of the ion. At large distances it is given by

$$\lim_{r\to\infty} V_{ia}(r) = -\frac{C_4}{r^4}, \tag{1}$$

with $C_4 = e^2\alpha_p/2$. Here e is the charge of the ion and α_p is the static polarizability of the atom. It is useful to introduce the length scale $R^* = \sqrt{2\mu C_4/\hbar^2}$ and the energy scale $E^* = \hbar^2/2\mu(R^*)^2$ that characterize the atom-ion potential, with μ the reduced mass. For the atom-ion combinations studied in this work we have that $R^* = 306$ nm and $E^*/h = 935$ Hz for the atom-ion pair ^{87}Rb/^{171}Yb$^+$ [35] and $R^* = 75$ nm and $E^*/h = 133$ kHz for the atom-ion pair ^{7}Li/^{171}Yb$^+$ [36].

For $r \to 0$, Eq. (1) does not describe the potential anymore as it becomes strongly repulsive. The exact form of the potential in this regime is generally not known well enough to solve the scattering dynamics, but as it has been shown in Ref. [30], QDT can be employed to parametrize the potential at short range (see Ref. [31] for more details).

Although the potential (1) is clearly spherically symmetric, we will for now limit ourselves to the one-dimensional (1D) case and we will denote the position of the ion (atom) as z_i (z_a). We note that in one dimension it turns out that the atom-ion interaction has the same mathematical expression as in three dimensions, that is, $V_{ia}(z_i,z_a) = -C_4/(z_i - z_a)^4$ [30]. We discuss the 3D scenario in Appendix A and compare it to the 1D results.

As an illustration of the atomic dynamics in a double-well system in the presence of an ion, we first solve the system assuming that the ion is pinned to the center of its trap at $z_i = 0$. Hence, the Hamiltonian of the atom is

$$H_a = \frac{p_a^2}{2m_a} + V_{\mathrm{DW}}(z_a) - \frac{C_4}{z_a^4}, \tag{2}$$

with p_a the momentum of the atom, m_a the atomic mass, and $V_{\mathrm{DW}}(z_a)$ the double-well potential. A convenient choice for $V_{\mathrm{DW}}(z_a)$ is given by

$$V_{\mathrm{DW}}(z_a) = \frac{b}{d^4}\left(z_a^2 - d^2\right)^2. \tag{3}$$

This potential has minima at $z_a = \pm d$ with local trapping frequencies $\omega_a = \sqrt{8b/m_a d^2}$ and interwell barrier b. For the sake of simplicity and without loss of generality, we fix the local trapping frequency ω_a for each interwell distance $2d$ by setting $b = \omega_a^2 m_a d^2/8$.

Our goal is to find a set of basis functions to expand the solution of H_a onto, as this procedure is more efficient than solving the Schrödinger equation for each d separately. To this end, we write the Hamiltonian as $H_a = H_a^{(0)} + H_a^{(1)}$ with

$$H_a^{(0)} = -\frac{\hbar^2}{2m_a}\frac{\partial^2}{\partial z_a^2} + \frac{1}{2}m_a\omega_a^2 z_a^2 - \frac{C_4}{z_a^4}, \tag{4}$$

$$H_a^{(1)} = \frac{1}{8}m_a\omega_a^2\left(d^2 - 2z_a^2 + \frac{z_a^4}{d^2}\right) - \frac{1}{2}m_a\omega_a^2 z_a^2. \tag{5}$$

Note that the term $m_a\omega_a^2 z_a^2/2$ has been added to (4) and subtracted again in Eq. (5). This allows for finding a set of discrete basis states instead of the continuum that arises without this term for $E > 0$. This is convenient as the final solutions of H_a will form a discrete set as well [13].

To solve the Schrödinger equation for $H_a^{(0)}$ by means of QDT, we note that as $z_a \to 0$ the energy is dominated by the term $-C_4/z_a^4$. Therefore, we can neglect the other energies and solve the Schrödinger equation analytically. We obtain even and odd solutions given by [30]

$$\tilde{\psi}_e(z_a) \propto |z_a| \sin\left(\sqrt{\frac{m_a}{\mu}}\frac{R^*}{|z_a|} + \phi_e\right), \tag{6}$$

$$\tilde{\psi}_o(z_a) \propto z_a \sin\left(\sqrt{\frac{m_a}{\mu}}\frac{R^*}{|z_a|} + \phi_o\right), \tag{7}$$

where ϕ_e and ϕ_o are the even and odd short-range phases, respectively. Since the short-range phases are not generally known experimentally and cannot be reliably obtained from

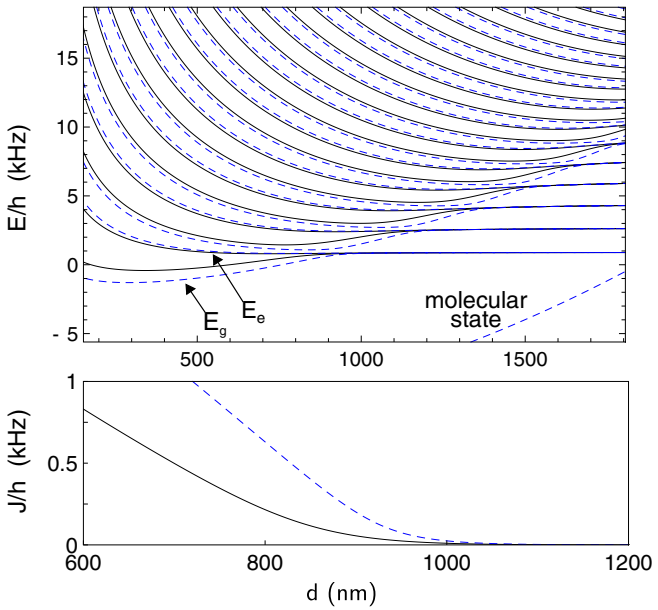

FIG. 2. (Color online) The top panel shows the eigenenergy spectrum as a function of the interwell separation d for ^{87}Rb and $^{171}Yb^{+}$ assuming $\phi_e = -\pi/4$, $\phi_o = \pi/4$ (black solid lines) and $\phi_e = -\pi/3, \phi_o = \pi/3$ (blue dashed lines). For large well separations, the spectrum resembles that of two independent harmonic oscillators of the same trap frequency $\omega_a = 2\pi \times 1.8$ kHz. As the wells approach, each level splits in two owing to the energy difference of even and odd wave functions. In the right corner a molecular state can also be seen. The occurring tunneling rate is given by the energy difference and is plotted in the bottom panel.

ab initio calculations, we choose a number of realistic values here, corresponding to scattering lengths in the range $-R^*$ to R^*. We also note that in a quasi-1D setup the values of the phases can be tuned by changing the confinement in the two remaining dimensions [30].

In order to solve the Schrödinger equation for the Hamiltonian (4), we use Eqs. (6) and (7) as a boundary condition at some small value $z_{\min}$ such that $C_4/z_{\min}^4 \gg E_{\max}$, with $E_{\max}$ being the largest energy considered in the problem. A renormalized Numerov method [37] gives the solutions $\Phi_k^{(0)}(z_a)$ with energies $\mathcal{E}_k^{(0)}$ and quantum number k. To solve the dynamics in the double well we now diagonalize the Hamiltonian with matrix elements

$$H_{kk'} = \left(E_k^{(0)} + \frac{m_a\omega_a^2 d^2}{8}\right)\delta_{kk'} + \frac{m_a\omega_a^2}{4}\left(\frac{\mathcal{M}_{kk'}^{(4)}}{2d^2} - 3\mathcal{M}_{kk'}^{(2)}\right),$$

$$\mathcal{M}_{kk'}^{(j)} = \int \Phi_k^{(0)}(z_a) z_a^j \Phi_k^{(0)}(z_a) dz_a,$$

with $j = 2,4$ for a range of values d.

Now, as in our previous study [13], we consider ^{87}Rb and $^{171}Yb^{+}$ as an example system and we assume that no spin-changing collisions can occur such that our single-channel description is accurate. Setting $\omega_a = 2\pi \times$ 1.8 kHz, we obtain the spectrum shown in Fig. 2. For large interwell separations d the eigenenergies resemble the equidistant level structure of the harmonic oscillator as the wells are uncoupled. While decreasing the interwell distance, the energy levels split in two as there is an energy difference between states of even and odd symmetry. For a single atom and small energy splitting, this energy difference corresponds to the interwell tunneling rate in a two-mode picture [38]. Since the barrier height b decreases with distance, the higher excited atomic states exhibit level splitting at larger separation d than low-energy states. The eigenenergies that asymptotically connect to the harmonic-oscillator ground states correspond to superpositions of approximately localized wave packets: $\Phi_{e,g}(z_a) = [\Phi_L(z_a) \pm \Phi_R(z_a)]/\sqrt{2}$ in the left L and right R well. These states are labeled with the subscripts g and e and have energies $E_{e,g}$ with $E_e \geqslant E_g$. At $d = 900$ nm we find that the ground-state degeneracy is lifted corresponding to a tunneling rate of $J/h = (E_e - E_g)/h = 56$ Hz when $\phi_e = -\pi/4$, $\phi_o = \pi/4$ (black lines) and $J/h = 202$ Hz when $\phi_e = -\pi/3$, $\phi_o = \pi/3$ (dashed blue lines). Since the short-range phases depend on the relative spin orientations of the atom and ion, the above calculation demonstrates an ion spin dependence similar to that in Ref. [13]. Finally, we note that the spectrum was obtained by taking 106 basis states into account.

In Appendix A we perform a 3D analysis of the double well for a static ion that we compare to the 1D model of the present section. We show that the double-well problem in one dimension has a strict analogy to the 3D scenario and therefore it provides a satisfactory physical picture of the system. Given this, we extend our analysis to the case of a moving ion. A 3D study of such a system would indeed be rather difficult to treat numerically and nonetheless it would not provide further insight into the problem.

III. A MOVING ION

Now we will see how the picture is altered when we allow the ion to move. As outlined above, we will restrict our attention to the 1D scenario. In this case the Hamiltonian is given by

$$H = \frac{p_i^2}{2m_i} + \frac{p_a^2}{2m_a} + \frac{1}{2}m_i\omega_i^2 z_i^2 + V_{\mathrm{DW}}(z_a) - \frac{C_4}{(z_i - z_a)^4}. \tag{8}$$

Here ω_i denotes the ion trap frequency, m_i the mass of the ion, and p_i its momentum. To find the eigenstates and energies of this Hamiltonian, we write the Hamiltonian in terms of relative and center-of-mass coordinates $r = z_i - z_a$ and $R = (m_i z_i + m_a z_a)/M$ with $M = m_i + m_a$ the total mass, as $H^{(d)} = H_R^{(0)} + H_r^{(0)} + H^{(1)}$:

$$H_R^{(0)} = -\frac{\hbar^2}{2M}\frac{\partial^2}{\partial R^2} + \frac{1}{2}M\omega_R^2 R^2, \tag{9}$$

$$H_r^{(0)} = -\frac{\hbar^2}{2\mu}\frac{\partial^2}{\partial r^2} + \frac{1}{2}\mu\omega_r^2 r^2 - \frac{C_4}{r^4}, \tag{10}$$

$$H^{(1)} = \mu\left(\omega_i^2 - \omega_a^2\right)Rr + V_{\mathrm{DW}}(R,r) - \frac{\mu\omega_a^2}{2}\left(\frac{m_a}{\mu}R^2 + \frac{\mu}{m_a}r^2 - 2Rr\right). \tag{11}$$

Equation (9) denotes the Hamiltonian of a harmonic oscillator with trap frequency $\omega_R^2 = (m_i\omega_i^2 + m_a\omega_a^2)/M$. It has eigenstates $f_n(R)$ and energies $E_n^{(0)} = \hbar\omega_R(n + 1/2)$.

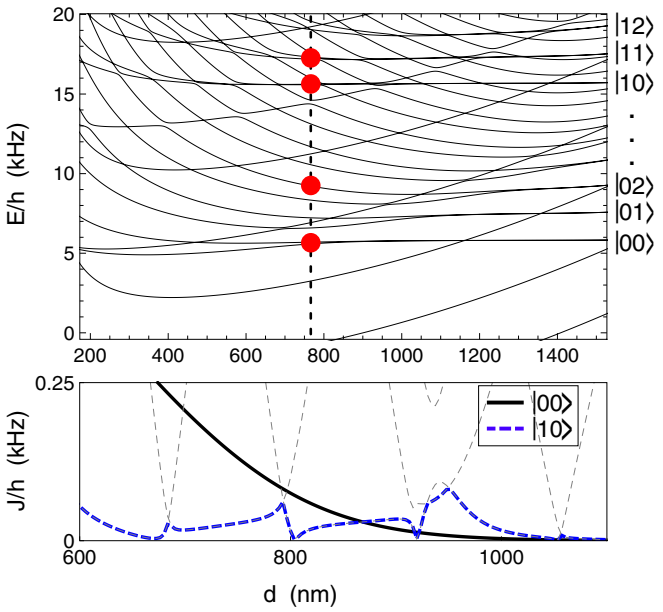

FIG. 3. (Color online) The top panel shows the spectrum of a double-well system where the ion is allowed to move for ^{87}Rb and ^{171}Yb^{+} with $\omega_a = 2\pi \times 1.8$ kHz, $\omega_i = 2\pi \times 9.9$ kHz, $\phi_e = -\pi/4$, and $\phi_o = \pi/4$. On the right we give some of the asymptotic quantum numbers $|n_i,n_a\rangle$ for large well separation. The red dots correspond to the wave functions plotted in Fig. 5. In the bottom panel the level splitting is plotted for the case where the ion is in the ground state (thick black solid line) and for the case where it is in the first excited state (dashed lines). When avoided crossings occur, the energy-level separation becomes dependent on whether the crossing is traversed diabatically or adiabatically. The smallest J is plotted using a thicker dashed blue line. Close to the avoided crossings, the two-mode description is no longer accurate and J loses its interpretation as the tunneling rate.

Equation (10) is similar to Eq. (4) except for some prefactors, in particular $\omega_r^2 = (m_i\omega_a^2 + m_a\omega_i^2)/M$. As explained in the previous section, we have determined the eigenfunctions $\Phi_k^{(0)}(r)$ and eigenenergies $\mathcal{E}_k^{(0)}$ of such a Hamiltonian by means of QDT. To find the eigenstates and eigenenergies to the full Hamiltonian we expand onto the basis $|f_n,\Phi_k^{(0)}\rangle$. We denote the solutions for each interwell separation d as $\psi_l^{(d)}(R,r) = \sum_{nk} c_{lnk}^{(d)} f_n(R)\Phi_k^{(0)}(r)$ with energies $E_l^{(d)}$ and coefficients $\mathbf{c}_{lnk}^{(d)}$, where an overall quantum number l labels each solution.

A. Examples

As an example of the resulting spectrum we show the situation for ^{87}Rb and ^{171}Yb^{+} assuming $\phi_e = -\pi/4$, $\phi_o = \pi/4$, $\omega_a = 2\pi \times 1.8$ kHz, and $\omega_i = 2\pi \times 9.9$ kHz in Fig. 3. This spectrum was obtained by expanding the solutions onto 6417 basis states (93 states in the relative coordinate and 69 states in the center-of-mass coordinate). In comparison to Fig. 2 we see that more energy levels appear, in the form of both molecular states and trap states. When the wells are far apart, the states reduce to the harmonic-oscillator states for the atom and ion. We can identify the asymptotic atom-ion Fock states $|n_i,n_a\rangle$ in Fig. 3 for large d. For intermediate d, the states are perturbed by the atom-ion interaction.

Focusing on the states that connect to the harmonic-oscillator ground states $|00\rangle$, we see the same behavior as for the case where the ion was static: The initial degeneracy for large interwell separations is lifted as the wells come closer and a tunneling rate can be identified. Molecular states cross the ground states at a few points, but the avoided crossings are very small. Therefore, the static ion approximation was justified when considering the ground states.

The state connecting to $|10\rangle$ shows a similar behavior, but more and larger avoided crossings appear. Close to these crossings, a simple two-mode picture breaks down and the tunneling rate J loses its meaning. In an experiment, the interwell separation d would typically be reduced dynamically to initiate tunneling. The resulting tunneling rate then depends on whether the crossing is traversed diabatically or not. For most values of d, the energy splitting is different than for the case when the ion is in the ground state. For $d = 775$ nm, for instance, we get a tunneling rate of $J/h = 101$ Hz when the ion is in the ground state, but only $J/h = 37$ Hz when the ion is in the first Fock state. Therefore, the atomic tunneling rate depends on the motional state of the ion.

As a second example, we also plot the case for ^{7}Li and ^{171}Yb^{+} assuming $\phi_e = -\pi/4$, $\phi_o = \pi/4$, $\omega_a = 2\pi \times 1.8$ kHz, and $\omega_i = 2\pi \times 9.9$ kHz (see Fig. 4). We see that the tunneling occurs for larger interwell separations for these

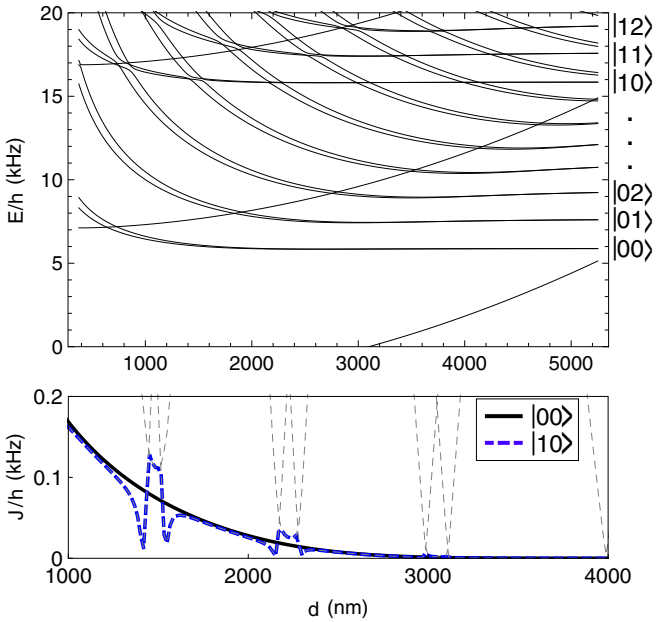

FIG. 4. (Color online) The top panel shows the spectrum of a double-well system where the ion is allowed to move for ^{7}Li and ^{171}Yb^{+} with $\omega_a = 2\pi \times 1.8$ kHz, $\omega_i = 2\pi \times 9.9$ kHz, $\phi_e = -\pi/4$, and $\phi_o = \pi/4$, i.e., the same parameters as in Fig. 3. Note that tunneling occurs for larger distances than for ^{87}Rb as the ^{7}Li wave packet is larger for the same trapping frequency. On the right we give the asymptotic quantum numbers $|n_i,n_a\rangle$ for large well separation. The bottom panel shows the energy-level separation J for the ion in the ground state (black solid line) and the first excited state (blue dashed line). The avoided crossings are also indicated by the thin gray lines. Clearly, in this case the tunneling rate is very similar for the first excited and ground states when no avoided crossings are near.

species as the atomic wave packet is larger because of its lower mass. Furthermore, the tunneling rate shows less dependence on the motional state of the ion as long as there are no avoided crossings nearby. This is a consequence of the large mass ratio between the atom and ion that separates atomic and ionic dynamics in a similar fashion as in the Born-Oppenheimer approximation. We note that in this case 2700 states were taken into account.

In Fig. 5 we plot a few probability distributions for the eigenstates corresponding to the red dots in Fig. 3. We see that for $z_a \sim z_i$, the atom-ion interaction dominates, but for larger atom-ion distances the probability distributions resemble those of the harmonic oscillator in each well and the presence of the ion only slightly perturbs the double-well system.

B. Controlling tunneling with nonclassical states of ion motion

An interesting application using the dependence of the tunneling rate on the motional state of the ion is the generation of entanglement between the atom and the ion. In Ref. [13] the state-dependent tunneling was proposed via the state dependence of the short-range phase. Alternatively, we can create nonclassical states of ion motion, such as Fock states, to engineer motional state-dependent tunneling. The Fock state can in turn be entangled with the spin of the ion. Such quantum states are commonly engineered and analyzed in ion trap experiments [39,40]. We note that such atom-ion entanglement production has various and interesting applications, for instance, in quantum metrology or in the investigation of the quantum-to-classical transition. Furthermore, by monitoring the entanglement dynamics one could measure the tunneling rate J and therefore infer scattering properties of the hybrid atom-ion system such as the corresponding s-wave scattering length.

From the spectrum displayed in Fig. 3, we see that a good strategy to engineer atom-ion entanglement consists of the following steps.

(i) We first prepare the ion in an equal superposition of the ground and first excited state of its trap, while its internal state is prepared in a specific hyperfine level.

(ii) Subsequently, we prepare the atom, for instance, in the ground state of the left well and far away from the ion such that the tunneling is negligible.

(iii) Then we reduce the interwell separation d dynamically until tunneling occurs.

(iv) Afterward, we wait until the atom has tunneled to one side depending on the ion Fock state, that is, to the right well if the ion Fock state is $|0\rangle$ and back to the left well if the ion Fock state is $|1\rangle$ (see Fig. 3, the first and third red dots from the bottom).

For the ion in the ground state $n_i = 0$, we see that the sequence is very similar to the one presented in Ref. [13] (see Fig. 3). For higher Fock states, however, we see an increasing amount of avoided crossings. To pass these crossings diabatically during our sequence, an accurate control of the interwell distance $d(t)$ is required. We see that for $n_i = 1$ the number of crossings is still quite limited and we take this as an example. We have performed numerical simulations of the dynamics and we have optimized the process, by means of the chopped random-basis algorithm [41], in order to maximize

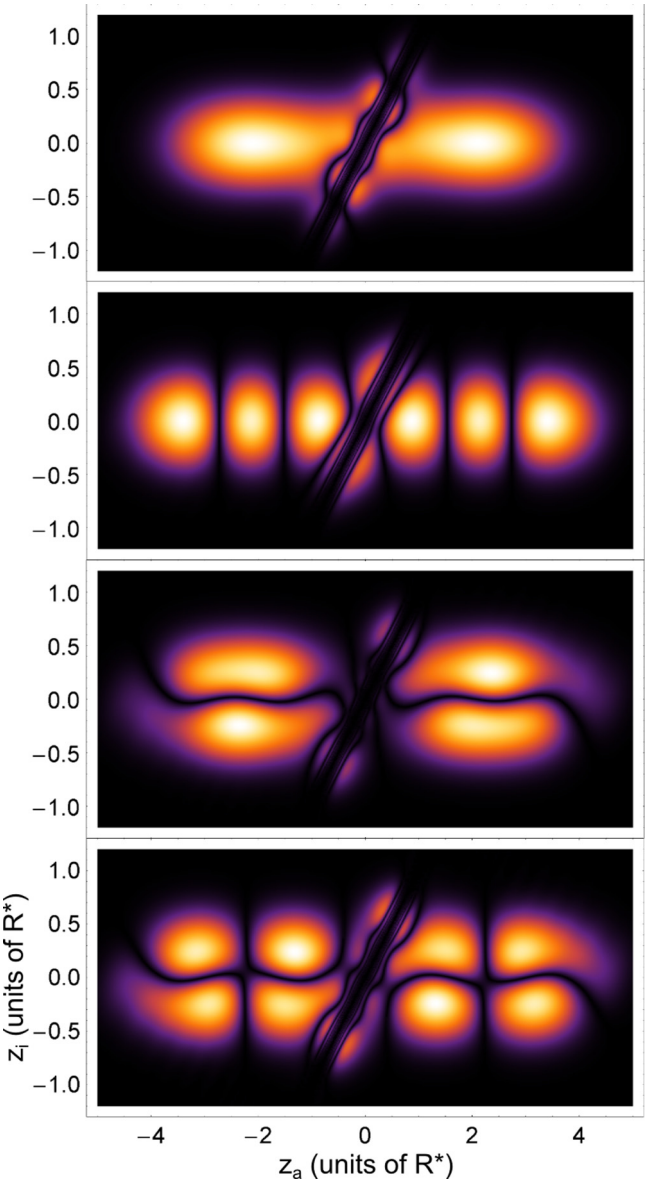

FIG. 5. (Color online) Wave functions $|\psi_l^{(d)}(z_i,z_a)|$ of the ion-atom states for an interwell separation of $d = 2.5R^*$=765 nm for ^{87}Rb and ^{171}Yb$^+$ with $\phi_e = -\pi/4$, $\phi_o = \pi/4$, $\omega_a = 2\pi \times 1.8$ kHz, and $\omega_i = 2\pi \times 9.9$ kHz, corresponding to the red dots in Fig. 3. We used units of R^* on the axes as these are the natural units for the atom-ion system. The states asymptotically correspond to the Fock states $|n_i,n_a\rangle = |00\rangle$, $|02\rangle$, $|10\rangle$, and $|11\rangle$ for large well separation (with the atom occupying both wells). The top wave function is the double-well ground state $|\Phi_g\rangle$. The corresponding quantum numbers can still be recognized by counting the nodes in the direction of the ionic and atomic coordinates. In the vicinity of the line $z_a = z_i$ the atom-ion interaction potential dominates and the wave functions take forms similar to Eqs. (6) and (7). The fast oscillations around this region are not completely resolved in the density plot.

the entanglement. To this aim, we have defined the following overlaps:

$$O_0(t) = \left|\langle\psi_{R,0}^{(0)}|\psi_{L,0}(t)\rangle\right|^2,$$
$$O_1(t) = \left|\langle\psi_{L,1}^{(0)}|\psi_{L,1}(t)\rangle\right|^2. \quad (12)$$

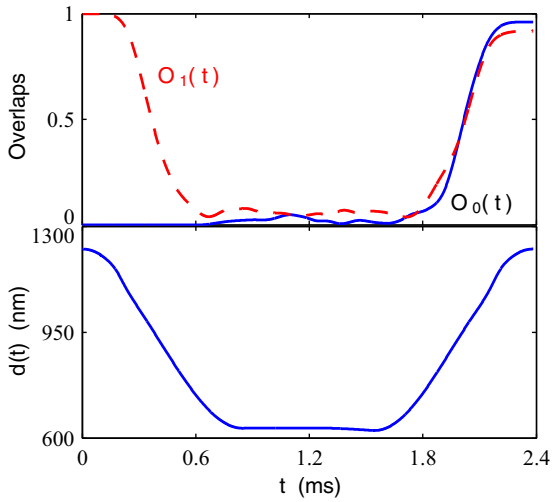

FIG. 6. (Color online) Optimization of the entanglement generation protocol as discussed in the main text. The top panel shows the overlaps $O_{0,1}(t)$ for the optimized dynamics. The bottom panel shows the optimal interwell separation. The optimization has been performed for the atom-ion pair ^{87}Rb/^{171}Yb^{+} with $\phi_e = -\pi/4$ and $\phi_o = \pi/4$.

Here $|\psi^{(0)}_{R,0}\rangle$ is the wave function of the atom in the ground state of the right well and the ion in the ground state of its harmonic trap, whereas $|\psi^{(0)}_{L,1}\rangle$ is the wave function of the atom in the ground state of the left well and the ion in the first excited state of its harmonic trap. The time-evolved states are obtained from $|\psi_{L,0}(t)\rangle = U(t)|\psi^{(0)}_{L,0}\rangle$ and $|\psi_{L,1}(t)\rangle = U(t)|\psi^{(0)}_{L,1}\rangle$, where $U(t)$ is the time-evolution operator generated by the Hamiltonian (8). In the optimization procedure we minimized the overlap infidelity $2 - O_0(T) - O_1(T)$ at the final time T, that is, the time needed to perform the sequence (iii) to (iv) outlined above, by optimally controlling the interwell separation $d(t)$. In Fig. 6 we show the overlaps $O_{0,1}(t)$ for the optimal interwell separation $d(t)$. We obtained $O_0(T) \simeq 0.96$ and $O_1(T) \simeq 0.92$ with $T \simeq 2.38$ ms for the atom-ion pair ^{87}Rb/^{171}Yb^{+}. This result shows that we can produce atom-ion entanglement in a very short time by means of the ionic motional state. We note, however, that the overlaps are not perfect. This might be achieved by controlling, for instance, the atom-ion interaction via Feshbach resonances or by controlling additionally the height of the barrier. Our goal here, however, is to show that such entanglement generation is in principle possible. A more detailed analysis by means of optimal control theory would require perfect knowledge of the trapping potentials and not just the analytically convenient form given by Eq. (3).

C. Imperfect ground-state cooling

Up until now, we have assumed that both the atom and the ion are prepared in a pure state by ground-state cooling (for instance, via resolved sideband cooling) followed by coherent-state manipulation. To see what the effect of imperfect ground-state cooling of the ion would be, we have plotted in Fig. 7 the spectra for the first five states that asymptotically correspond to

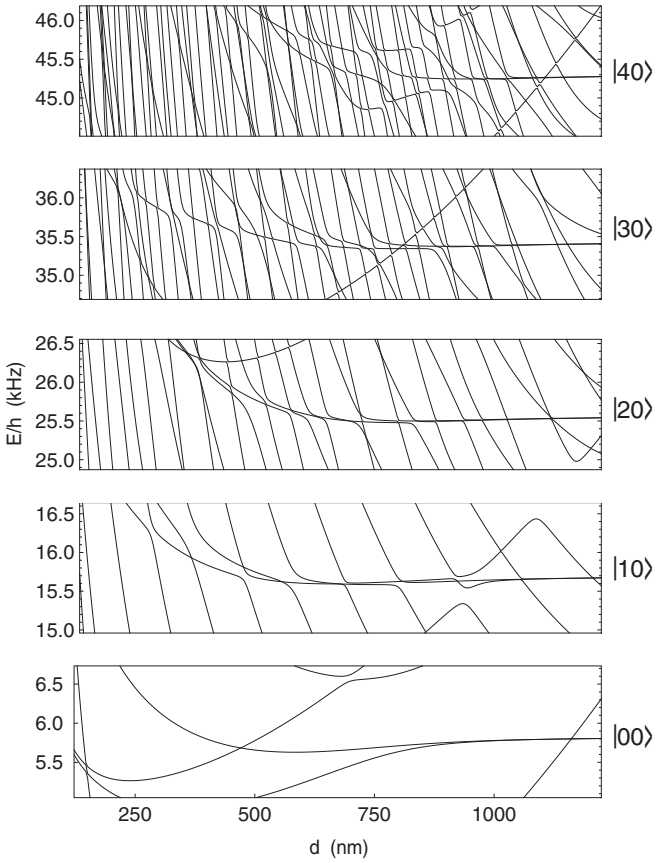

FIG. 7. Enlarged view of the five first Fock states of the ion in the spectrum of a double well with moving ion for ^{87}Rb and ^{171}Yb^{+} with $\phi_e = -\pi/4$, $\phi_o = \pi/4$, $\omega_a = 2\pi \times 1.8$ kHz, and $\omega_i = 2\pi \times 9.9$ kHz.

the first five Fock states of the ion. When the ion is in a thermal state, each of these Fock states contributes to the tunneling rate in a incoherent manner. We see that for $n_i = 0, \ldots, 3$ the energy levels display degeneracy in $|\Phi_{e,g}\rangle_{n_i}$ for large d, in analogy to the situation for the ground states discussed above. As the interwell separation is decreased these degeneracies are lifted and tunneling occurs. Because of the coupling between the atomic tunneling and the motion of the ion, each ionic state corresponds to a different tunneling rate. Unless only few Fock states are occupied in the thermal state or the tunneling rates are very similar for all Fock states, the coherence in the atomic state will be destroyed after a while.

For the states of higher energy $n_i \geqslant 3$ we see that many avoided crossings start appearing that cannot be ignored anymore for small d. In this situation, the simple two-mode picture cannot be employed anymore.

As an example, we have focused our attention on the tunneling only, in particular when the ion is (ideally) prepared in the ground state. To this end, we performed first an optimization of this dynamics. The corresponding result is shown in Fig. 8. In this case we were able to achieve an overlap fidelity of about $O_0(T) \simeq 0.99$ in $T \simeq 2.38$ ms. Given this result, we have investigated the impact of finite temperature on the tunneling dynamics. To begin with, we have defined the

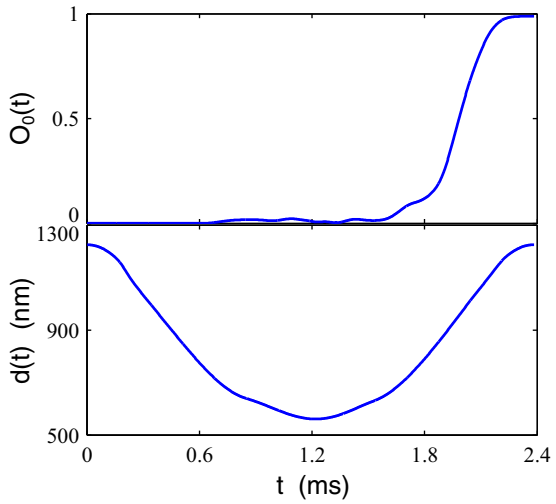

FIG. 8. (Color online) Optimization of the tunneling dynamics when the ion is prepared in the ground state. The top panel shows the overlap $O_0(t)$ for the optimized dynamics. The bottom panel shows the optimal interwell separation. The optimization has been performed for the atom-ion pair ^{87}Rb/^{171}Yb$^+$ with $\phi_e = -\pi/4$ and $\phi_o = \pi/4$. The final overlap fidelity is $O_0(T) \simeq 0.99$.

initial density matrix of the ion as

$$\rho_i(\mathcal{T}) = \sum_{n_i} p_{n_i}(\mathcal{T})|n_i\rangle\langle n_i|, \tag{13}$$

where $|n_i\rangle$ are the harmonic-oscillator eigenstates of the ionic harmonic trap and $p_{n_i}(\mathcal{T})$ are the occupation probabilities that are calculated by assuming a thermal distribution corresponding to temperature $\mathcal{T}$ in the canonical ensemble. The overlap fidelity at time $t = T$ for a given temperature is given by

$$F(\mathcal{T}) = \sum_{n_i} p_{n_i}(\mathcal{T})\left|\langle\psi_{R,n_i}|\psi_{L,n_i}(t)\rangle\right|^2. \tag{14}$$

Here $|\psi_{L,n_i}(t)\rangle$ is the time-evolved state assuming that the initial state is the ground state of the left well for the atom and the nth state of the harmonic trap for the ion.

It is interesting to see values of the fidelity for temperatures up to $k_B\mathcal{T} \approx \hbar\omega_i$ (k_B is the Boltzmann constant). Let us define $\gamma = \exp(-\hbar\omega_i/k_B\mathcal{T})$ and neglect terms of $o(\gamma^5)$ in Eq. (14), since for higher energies the motional states of the atom and the ion are no longer separable. Such temperature dependence of the fidelity is displayed in Fig. 9, for which we used the optimal interwell separation shown in the bottom panel of Fig. 8. As shown, the fidelity drops rather quickly since the overlaps at time T for the ionic states $n_i = 1,2,3,4$ are significantly reduced. This shows that the tunneling rates are different for those Fock states and therefore the coherence in the atomic state is destroyed rapidly.

A strategy to reduce the impact of finite temperature could be to perform an optimization in which the optimal interwell separation $d(t)$ is engineered in such a way that $F(\mathcal{T})$ is maximized within a given temperature range.

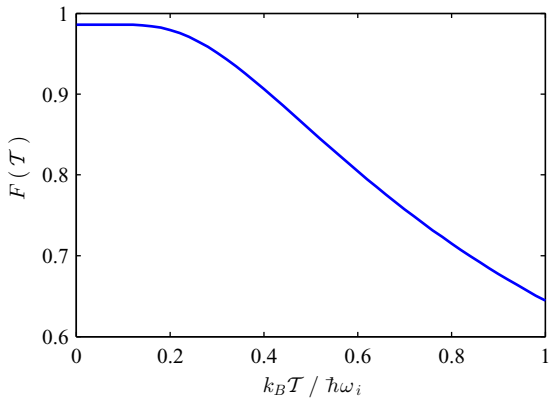

FIG. 9. (Color online) Fidelity $F(\mathcal{T})$ of the tunneling dynamics for the atom-ion pair ^{87}Rb/^{171}Yb$^+$, whose overlap fidelity when the ion is prepared in the ground state of the trap and the corresponding optimal interwell separation are displayed in Fig. 8.

IV. MICROMOTION

So far, we have assumed that the ion is trapped in a time-independent harmonic trap. In most atom-ion experiments, however, the ions are trapped in a Paul trap that is based on an oscillating electric field. This causes a rapid oscillating motion of the ion called micromotion.

The Hamiltonian describing this situation in one dimension is given by

$$H_{\text{ion}}(t) = \frac{p_i^2}{2m_i} + \frac{1}{8}m_i\Omega^2 z_i^2[a + 2q\cos(\Omega t)]. \tag{15}$$

Here the parameters a and q depend on the trapping potential, the ion mass, and its charge. With properly chosen a and q, an effective time-independent trapping potential can be derived via the so-called secular approximation. In this approximation the ion motion reduces to a combination of the slow (secular) motion, that is, of a particle in a time-independent trap and a rapid micromotion of small amplitude. In most experiments the following inequalities hold: $a \ll q < 0.91$, where q lies typically in the range 0.1–0.4.

In order to evaluate the impact of the time-dependent ion trap on the double-well system, we replace the ion trap term (i.e., the kinetic and trapping potential energies) in Eq. (8) by the time-dependent version of Eq. (15). Nguyen *et al.* [32] have analyzed a situation in which the atom was trapped in a harmonic trap. Here we use the same approach, but for a double-well potential. We perform the transformation of Cook *et al.* [32,42] to obtain a Hamiltonian that is comprised of a time-independent and a time-dependent term that we label with *mm* (micromotion): $H_{\text{tot}} = H^{(d)} + H_{mm}(t)$. Note that $H^{(d)}$ is the Hamiltonian of the double well without micromotion, which is defined in Eqs. (9)–(11). More details on this procedure can be found in Appendix B. The micromotion Hamiltonian in the center-of-mass and relative coordinates is

given by

$$H_{mm}(t) = -m_i g^2 \omega_i^2 \left(R^2 + \frac{\mu^2}{m_i^2} r^2 + \frac{2\mu}{m_i} r R \right) \cos 2\Omega t - g\omega_i \left(\{R,p\} + \frac{\mu}{m_i}\{r,p\} + \frac{m_i}{M}\{R,P\} + \frac{\mu}{M}\{r,P\} \right) \sin \Omega t. \quad (16)$$

Here $g = [2(1 + 2a/q^2)]^{-1/2}$ and $\{\cdot,\cdot\}$ denotes the anticommutator. The relative and center-of-mass momenta are denoted by p and P, respectively.

Following again Ref. [32], we use Floquet theory to obtain the energies and eigenstates in terms of the unperturbed eigenstates of the Hamiltonian $H^{(d)}$. It turns out that we have to diagonalize the Hamiltonian

$$H_F = H^{(d)} + H_{mm}(t) - i\hbar \frac{\partial}{\partial t}. \quad (17)$$

We use the unperturbed Floquet eigenstates $|u_{jl}\rangle = e^{ij\Omega t}|\psi_l^{(d)}(R,r)\rangle$ of $H_F - H_{mm}(t)$ as our basis with Floquet energies $\epsilon_{jl} = E_l + j\hbar\Omega$. Here the integer j denotes the class of the Floquet state, whereas the quantum number l denotes the solution to the double-well problem without micromotion. Then we introduce the generalized matrix elements

$$\langle\langle u^*_{j'l'}|H_{mm}(t)|u_{jl}\rangle\rangle = \frac{1}{T}\int_0^T dt \langle u^*_{j'l'}|H_{mm}(t)|u_{jl}\rangle, \quad (18)$$

where now T indicates the period of the micromotion. To gain further insight into the micromotion effect we write the matrix elements as follows [32] (see Appendix B):

$$\langle u^*_{j'l'}|H_{mm}(t)|u_{jl}\rangle = \left\langle \psi_{l'}^{(d)} \right| [V_1 \cos(2\Omega t) + V_2 \sin(\Omega t)] e^{i(j-j')\Omega t} \left| \psi_l^{(d)} \right\rangle,$$
$$V_1 = -m_i g^2 \omega_i^2 \left(R^2 + \frac{m_a^2}{M^2} r^2 + \frac{2m_a}{M} R r \right), \quad (19)$$

$$V_2 = -\frac{i g \omega_i m_i}{\hbar}(E_{l'} - E_l)\left(R^2 + \frac{m_a^2}{M^2} r^2 + \frac{2m_a}{M} R r \right). \quad (20)$$

The larger these matrix elements are, the less we expect the secular approximation to hold. Additionally, the coupling between two states may become resonant for states belonging to different Floquet classes when $\epsilon_{j'l'} = \epsilon_{jl}$. We note that the selection rules for the coupling between different Floquet classes are given by $|j - j'| = 1$ for V_2 and $|j - j'| = 2$ for V_1 [see also Eq. (18)]. When the micromotion Hamiltonian cannot be considered a perturbation, the problem has to be solved by taking a large number of Floquet classes into account. However, for large interwell separation, we do not expect the micromotion to play a significant role as the atom is trapped too far away from the ion to sense the small-amplitude micromotion of the ion. As d is decreased, we expect the micromotion term to become increasingly important.

To quantify this, we study how strongly the micromotion couples the states of interest $|\Phi_{e,g}^{(d)}\rangle$ to states with a different energy as d is decreased. We limit the discussion to $|\Phi_g^{(d)}\rangle$ as it can be shown that the effects are very similar for $|\Phi_e^{(d)}\rangle$. The energy difference prefactor $(E_{l'} - E_l)$ causes V_2 to be the main perturbing term [32] and we focus on it from now on. Let us introduce the following notation for (the absolute value of) these matrix elements:

$$V_{rr} = \frac{g m_i \omega_i (E_g - E_l)}{\hbar} \frac{m_a^2}{M^2} \left| \langle \Phi_g^{(d)} | r^2 | \psi_l^{(d)} \rangle \right|,$$
$$V_{rR} = \frac{g m_i \omega_i (E_g - E_l)}{\hbar} \frac{m_a}{M} \left| \langle \Phi_g^{(d)} | r R | \psi_l^{(d)} \rangle \right|,$$
$$V_{RR} = \frac{g m_i \omega_i (E_g - E_l)}{\hbar} \left| \langle \Phi_g^{(d)} | R^2 | \psi_l^{(d)} \rangle \right|.$$

In Figs. 10(a)–10(c) the resulting matrix elements for the case discussed in Fig. 3 are shown (i.e., for the atom-ion pair ^{87}Rb/^{171}Yb$^+$). Here the matrix elements are plotted for $d = 1080$ and 820 nm and the detuning of the coupling state $E_g - E_l$. Clearly, the couplings are largest to states that are nearby in energy. For V_{RR}, the couplings quickly fall to zero as the coupling state is further separated in energy. The terms involving r and r^2, however, have significant couplings with states that are far separated in energy.

This behavior is a direct consequence of the nonlinear interaction between the atom and the ion. In the center-of-mass coordinate the basis functions are Fock states and the matrix elements involving only R have well-defined selection rules: $\langle f_{n'}|R|f_n\rangle \neq 0$ for $|n - n'| = 1$ and $\langle f_n|R^2|f_{n'}\rangle \neq 0$ for $|n - n'| = \{0,2\}$. Since the atomic and ionic ground states are only slightly perturbed by the atom-ion interaction, as is clear from Sec. III, few Fock states are involved and due to the selection rules only coupling to nearby states occur. Because there are also selection rules on j, the coupling states need to be of a different Floquet class. These states are unlikely to become resonant since $\Omega \gg \omega_R$. This situation is comparable to the effect that micromotion has on a single trapped ion. For the atom-ion scattering states in the relative coordinate, however, there are no selection rules owing to the nonlinear atom-ion interaction. For instance, $\langle \Phi_k|r^2|\Phi_{k'}\rangle \neq 0$ in general for any k and k' that have the same symmetry. Thus, the states of interest couple to highly excited states belonging to different Floquet classes.

For the case studied here, $\Omega = 2\pi \times$ 70.5 kHz, which corresponds to $q = 0.4$. For interwell distances of about 820 nm, the couplings to states that are ~70 kHz separated in energy—and can therefore become resonant—reach up to 10% of the atomic trapping frequency. Such large couplings cause significant deviations from the secular solution if resonances occur. This situation is indeed quite similar to the case studied in Ref. [32]. Hence, we expect a large number of energy levels crossing the ground states with increasing strength as d is reduced. This will render the state preparation more difficult when considering schemes where d is slowly reduced to initiate atomic tunneling. Only superb experimental control over $d(t)$ will allow the diabatic transfer over avoided crossings such that atomic excitations within the wells are prevented.

It is interesting to note that the prefactors to the terms containing r and r^2 in Eqs. (19) and (20), which will cause the largest effects, are $m_a/M = \mu/m_i$ and m_a^2/M^2, respectively. This suggests that adverse micromotion effects may be reduced

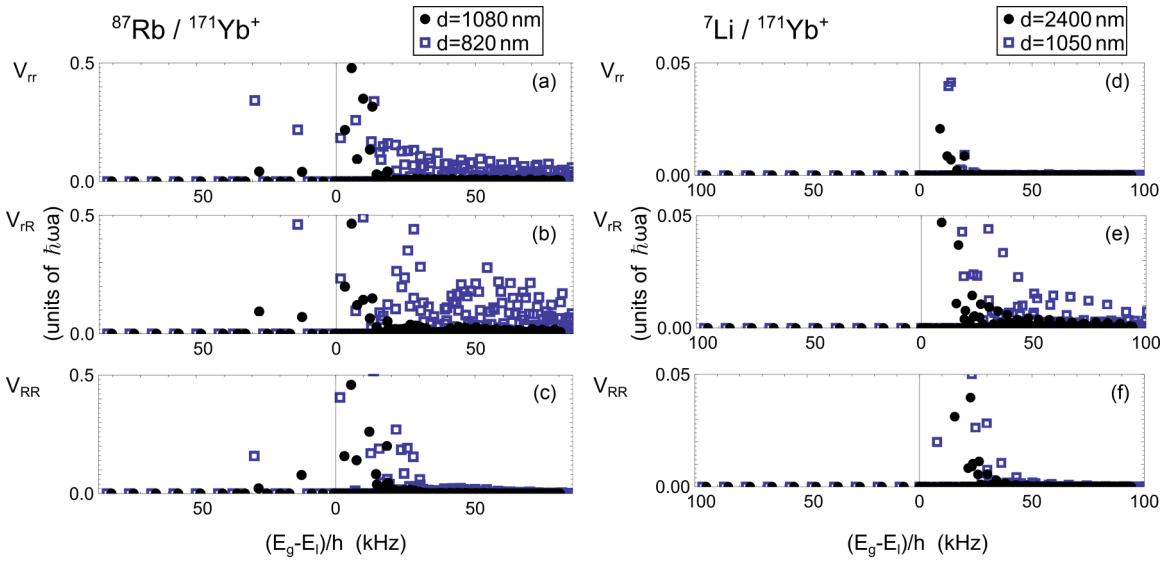

FIG. 10. (Color online) (a)–(c) Matrix elements V_{rr}, V_{rR}, and V_{RR}, respectively, in units of $\hbar\omega_a$ for ^{87}Rb and ^{171}Yb$^+$ with $\phi_e = -\pi/4$, $\phi_o = \pi/4$, $\omega_a = 2\pi \times 1.8$ kHz, and $\omega_i = 2\pi \times 9.9$ kHz for $d = 1080$ and 820 nm. The energy separation of the coupling state is plotted on the horizontal axis. Since stable ion trapping requires $\Omega \gtrsim 2\pi \times 30$ kHz (for $a = 0$), only states with detunings larger than this can cause resonances. It can be seen that the elements V_{rr} and V_{rR} couple states that are separated in energy by more than 30 kHz, whereas V_{RR} remains localized in energy such that it cannot cause resonant couplings. For interwell distances of $\lesssim$820 nm, the tunneling rate reaches $J/h = 58$ Hz, but the matrix elements of V_{rr} and V_{rR} already reach 10% of the atomic trapping frequency for energy differences around 85 kHz. Resonances with this strength would significantly affect the energy spectrum. This would render state preparation significantly more difficult and cause the two-mode approximation for the double-well to break down. (d)–(f) Matrix elements for ^{7}Li and ^{171}Yb$^+$ for $d = 2400$ and 1050 nm and the same trap frequencies. At $d = 1050$ nm we find a tunneling rate of $J/h = 150$ Hz, whereas the micromotion-induced couplings are at the percent level.

by choosing $m_i \gg m_a$, This observation is in line with the classical study of Cetina *et al.* [33] concerning the limits of atom-ion sympathetic cooling. As a comparison for the case of the double well, we plot also the matrix elements for the case of ^{7}Li and ^{171}Yb$^+$ [see Figs. 10(d)–10(f)]. We see that the matrix elements are indeed smaller for this case and we reach a tunneling rate of $J/h = 150$ Hz with micromotion-induced couplings on the percent level of the atomic trap frequency or ∼20 Hz.

Finally, we have numerically solved the full double-well problem including micromotion. The required total Hilbert space dimensions scale as $N_{\rm com} \times N_{\rm rel} \times N_{\rm echos}$, that is, the number of center-of-mass states to be taken into account times the number of relative states times the number of Floquet classes. Clearly, the calculation becomes very hard already at small d. For instance, calculating the eigenenergies for the case presented in Fig. 3 taking only the classes $j = -2, \ldots, 2$ into account would require a Hilbert space of dimension 32 000 × 32 000. For the case of ^{7}Li and ^{171}Yb$^+$ of Fig. 4 the situation is better and we diagonalize the Hamiltonian for 500 values of d taking $j = -2, \ldots, 2$ such that 13 500 states are used to form the basis. The result is shown in Fig. 11(a). We can see that although many more energy levels are present in the spectrum, the coupling to the states $|\Phi^{(d)}_{e,g}\rangle$ is indeed very small, so the micromotion should not pose a problem for the parameters considered here.

As a second example we calculate the spectrum around the ground states for a higher trap drive frequency. To reduce the numerical complexity we use ^{7}Li and ^{171}Yb$^+$ and set all energy scales to similar values, i.e., $\omega_a = 2\pi \times 98$ kHz and $\Omega = 2\pi \times 967$ kHz for $q = 0.4$ and $a = 0$ such that $\omega_i \approx 2\pi \times 137$ kHz; we obtain the eigenenergy spectrum shown in Fig. 11(b). For this calculation we took $j = -2, \ldots, 2$, $\phi_e = \pi/3$, and $\phi_o = -\pi/3$. Thus, the Hilbert space is comprised of 8640 basis states. As illustrated in Fig. 11, also for this case, we see that the avoided crossings remain relatively small and therefore enable us to apply the secular approximation for the double-well system at large enough separations d. Since the avoided crossings remain small, we do not expect that taking more Floquet classes into account will significantly alter the results for the values of d plotted. On the other hand, for smaller d, the ground state presents many avoided crossings and therefore more Floquet classes are required to reach convergence.

V. EXPERIMENTAL IMPLEMENTATION

Experiments combining ultracold atoms and ions have become available in recent years [1–5] studying cold collisions and chemistry as well as sympathetic cooling of ions by atoms. These have shown that inelastic collision rates can be low [2] such that coherent interactions between the two systems are within reach. The proposed double-well system requires combining trapped ions with atomic multiwell potentials that can be derived from either lasers or magnetic fields.

A. Optical potentials

Atomic double-well potentials have been created by using optical tweezers or standing-wave laser fields [14,17,18]. Such fields are sufficiently strong to also trap an ion, as it was shown in a recent proof-of-principle experiment [43]. An all optical

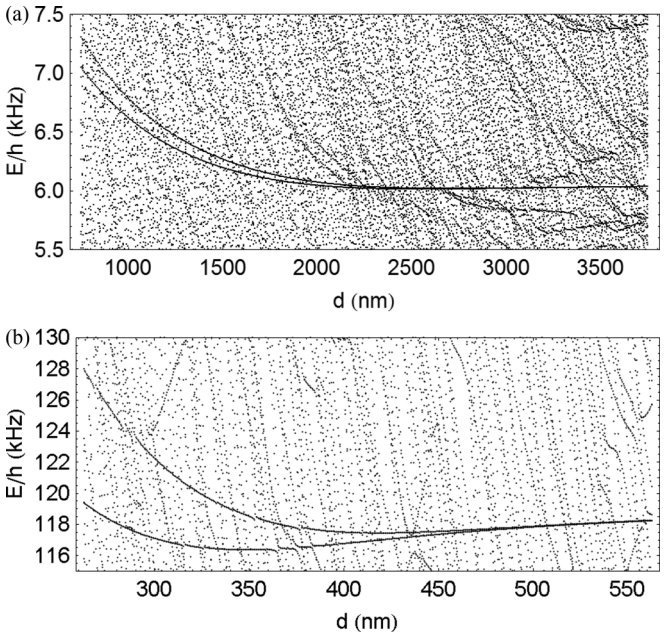

FIG. 11. (a) Spectrum around the states $|\Phi^{(d)}_{e,g}\rangle$ for ^{7}Li and ^{171}Yb$^+$ with $\omega_a = 2\pi \times 1.8$ kHz and $\Omega = 2\pi \times 70.5$ kHz for $q = 0.4$ and $a = 0$ such that $\omega_i \approx 2\pi \times 10$ kHz. For the calculation we took $j = -2, \ldots, 2$, $\phi_e = -\pi/4$, and $\phi_o = \pi/4$. To construct the basis 13 500 states were used. The Hamiltonian was diagonalized for 500 different values of d. It can be seen that many energy crossings appear, but the avoided crossings remain very small. (b) Spectrum for ^{7}Li and ^{171}Yb$^+$ with $\omega_a = 2\pi \times 98$ kHz and $\Omega = 2\pi \times 967$ kHz for $q = 0.4$ and $a = 0$ such that $\omega_i \approx 2\pi \times 137$ kHz. For the calculation we took $j = -2, \ldots, 2$, $\phi_e = \pi/3$, and $\phi_o = -\pi/3$. To construct the basis 8640 states were used. The Hamiltonian was diagonalized for 600 different values of d. It can be seen that many energy crossings appear and that the avoided crossings become bigger as d decreases.

or hybrid optical-Paul trap would solve the issues related to micromotion. In Ref. [44], for instance, a single ion was trapped in a standing-wave laser field. It is feasible to alter this setup to allow both a harmonic potential for the ions and a multiwell potential for the atoms by overlapping trapping beams of suitable frequencies. Hence, the system studied in this paper may be realized by using optical trapping fields or by means of a hybrid approach in which a Paul trap is combined with an optical one.

B. Microtraps

Atomic double-well systems have been created in atomic microtraps, or atom chips [45], where atoms are magnetically trapped by means of integrated current carrying wires [46–48]. Planar ion traps have also become available in recent years [49], whose development was mainly driven by the prospect of developing a scalable quantum computer [50,51]. It seems feasible to combine the technologies of atom chips and planar ion traps to implement the proposed setup. Recently, for instance, magnetic-field gradients were used in planar ion traps for spin detection or to design spin-spin interactions [52–56]. Those traps combine electrodes on the surface of a chip that form the ionic trap with current carrying wires to produce magnetic gradient fields. Gradients ranging from 1 to 20 T/m at $\sim$100 μm above the surface can be reached. Slight modifications to such a setup would lead to magnetic-field patterns that can trap atoms. For instance, we have calculated that by using a layered design, in which a planar ion trap is mounted on top of a current carrying structure, results in magnetic gradients of about 7 T/m. For atoms trapped 100 μm above the surface, this would correspond to trapping frequencies in the kilohertz range with appropriately aligned bias fields. Such a setup could be combined with radio-frequency fields as well, leading to adiabatic dressed double-well potentials, in analogy to the works of Refs. [19,21] and as described in more detail in Ref. [57]. In this setup, the interwell separation could be dynamically tuned by changing the frequency of the dressing field.

VI. CONCLUSION

We have studied theoretically the dynamics of an atomic double-well system in the presence of a single trapped ion. We have found, under the assumption that the ion is not moving, that a one-dimensional calculation provides the same physical picture as a three-dimensional one. The spin of the ion can control the tunneling rate via the state-dependent short-range phase, as also discussed in Ref. [13]. When the ion is allowed to move, we find that the atomic tunneling rate between the wells also couples to the ion motion. In this way, the tunneling can be controlled by the motion of the ion. As the motional state of trapped ions is routinely engineered and read out in state-of-the-art experiments [39,58] by coupling it to its internal (spin) state, this may allow engineering atom-ion states in which the atomic position is entangled with the ion motion or spin. We have analyzed a scheme in which the interwell distance is dynamically reduced to allow the atom to tunnel depending on the motional state of the ion. Imperfect ion ground-state cooling will result in reduced tunneling contrast. Since ion heating may occur on the time scale of the tunneling dynamics in experiments where the ion is trapped close to the electrodes, we plan to analyze the effect of ion heating and cooling on the tunneling dynamics in the future. The coupling between atomic tunneling and ion motion can also be seen as a unit cell for a larger atom-ion quantum simulator, in which the atomic dynamics is coupled to phonons in an ion crystal [26].

We have also analyzed the effect of micromotion on the energy spectrum of the double-well system. The micromotion causes many extra avoided crossings in the spectrum as coupling to states belonging to different Floquet classes becomes possible for small interwell separation d. The exact strength of these crossings depends on the trap parameters, but we conclude that it is a good idea to choose an ion-atom combination with a large mass ratio. The avoided crossings will cause trouble in state preparation as the wells have to be brought together diabatically with respect to the crossings, but without exciting the atoms to higher trap states. Additionally, the two-mode approximation may break down in a many-body scenario when including the micromotion, complicating its theoretical description.

In linear Paul traps, the dynamical electric field is only used to confine the ions in two of the three directions and it may be advisable to have the double-well separation in the third direction where the ion is confined by static fields.

Nonetheless, due to the spherical symmetry of the atom-ion interaction potential, there will be some minimum distance where the secular approximation will fail [32].

We have given two possible routes towards experimental implementation of the double-well system. The double-well potential is created either by using magnetic fields or with optical fields. Both technologies are compatible with ion trapping, putting an experimental realization of the considered system within reach.

ACKNOWLEDGMENTS

This work was supported by the ERC (Grant No. 337638) (R.G. and J.J.), an internal grant of the University Mainz (Project "Hybrid atom-ion microtrap") (R.G. and J.J.), and the excellence cluster The Hamburg Centre for Ultrafast Imaging–Structure, Dynamics and Control of Matter at the Atomic Scale of the Deutsche Forschungsgemeinschaft (A.N.). The authors acknowledge useful discussions with Andrew Grier and Krzysztof Jachymski and are grateful to Ferdinand Schmidt-Kaler, Tommaso Calarco, and Zbigniew Idziaszek for previous work on a related project. R.G. thanks Ulrich Poschinger for a critical reading of the manuscript.

APPENDIX A: THE 3D CALCULATION

The procedure for obtaining the 3D eigenenergies and states has been described in Ref. [13] and for completeness we give more details here. The 3D Hamiltonian is given by $H_{3D} = H_{3D}^{(0)} + H_{3D}^{(1)}$, where

$$H_{3D}^{(0)} = -\frac{\hbar^2\nabla_a^2}{2m_a} + \frac{1}{2}m_a\omega_\perp^2 r_a^2 - \frac{C_4}{r_a^4}, \tag{A1}$$

$$H_{3D}^{(1)} = V_{DW}(z_a) - \frac{1}{2}m_a\omega_\perp^2 z_a^2. \tag{A2}$$

Here $\omega_\perp$ is the trapping frequency in the transverse direction. We introduce spherical coordinates (r_a,θ_a,ϕ_a), where we keep the subscript a to denote the coordinates that belong to the atom. The solutions to the radially symmetric equation (A1) are of the form $\boldsymbol{\psi}_{nlm}^0(\mathbf{r}_a) = Y_l^m(\theta_a,\phi_a)\psi_{nl}^0(r_a)/r_a$, where $Y_l^m(\theta_a,\phi_a)$ are spherical harmonics and $\psi_{nl}^0(r_a)$ are the solutions to the radial Schrödinger equation. Since the potential does not depend on the azimuthal direction, the quantum number m is conserved and for simplicity we set $m = 0$.

The radial Schrödinger equation is given by

$$E_{nl}^{(0)}\psi_{nl}^0 = \left(-\frac{\hbar^2}{2m_a}\frac{\partial^2}{\partial r_a^2} + \frac{\hbar^2 l(l+1)}{2m_a r_a^2} + \frac{m_a\omega_\perp^2 r_a^2}{2} - \frac{C_4}{r_a^4}\right)\psi_{nl}^0.$$

To numerically solve this equation, we make use of the renormalized Numerov method [37] with

$$\tilde{\psi}_{nl}^0(r_a) \propto \sqrt{r}[J_{l+1/2}(\xi) + \tan(\delta)Y_{l+1/2}(\xi)] \tag{A3}$$

as a boundary condition, where $\xi = \sqrt{m_a/\mu}R^*/r_a$. The mixing angle δ is related to the 3D short-range phase as $\delta = -\phi - l\pi/2$. We then expand the solution of the full Hamiltonian H_{3D} onto the solutions of Eq. (A1), namely, $\boldsymbol{\psi}^{(d)}(\mathbf{r_a}) = \sum_k c_k\boldsymbol{\psi}_k^0(\mathbf{r_a})$, where k denotes the pair of quantum numbers (n,l). Thus, both the wave functions and the corresponding energies are obtained by diagonalizing the Hamiltonian H_{3D}, whose matrix elements are given by

$$H_{kk'} = \left(E_k^{(0)} + \frac{m_a\omega_a^2 d^2}{8}\right)\delta_{kk'} + \frac{m_a\omega_a^2}{4}\left(\frac{\mathcal{M}_{kk'}^{(4)}}{2d^2} - 3\mathcal{M}_{kk'}^{(2)}\right),$$

$$\mathcal{M}_{kk'}^{(j)} = \int d\mathbf{r}_a^3\boldsymbol{\psi}_{k'}^{0*}(\mathbf{r}_a)\cos^j(\theta_a)r_a^j\boldsymbol{\psi}_k^0(\mathbf{r}_a),$$

with $j = 2,4$. These matrix elements can be explicitly written as

$$\mathcal{M}_{nl,n'l'}^{(j)} = \int_0^\infty \psi_{n'l'}^{0*}(r_a)r_a^j\psi_{nl}^0(r_a)dr_a \times 2\pi\int_0^\pi \sin\theta_a\cos^j\theta_a Y_{l'}^*(\theta_a)Y_l(\theta_a)d\theta_a,$$

whose determination relies on the computation of the following Clebsch-Gordon coefficients:

$$C_{ll'}^{(j)} = 2\pi\int_0^\pi \sin\theta_a\cos^j\theta_a Y_{l'}^*(\theta_a)Y_l(\theta_a)d\theta_a,$$

$$C_{l,l}^{(2)} = \frac{2l(l+1)-1}{4l(l+1)-3},$$

$$C_{l,l+2}^{(2)} = \frac{(l+1)(l+2)\sqrt{5+4l(l+3)}}{(2l+1)(2l+3)(2l+5)},$$

$$C_{l,l}^{(4)} = \frac{3[3+2l(l+1)(l^2+l-4)]}{(2l-3)(2l-1)(2l+3)(2l+5)},$$

$$C_{l,l+2}^{(4)} = \frac{2(l+1)(l+2)[-3+2l(l+3)]\sqrt{5+4l(l+3)}}{(2l-1)(2l+1)(2l+3)(2l+5)(2l+7)},$$

$$C_{l,l+4}^{(4)} = \frac{(l+1)(l+2)(l+3)(l+4)\sqrt{9+4l(l+5)}}{(2l+1)(2l+3)(2l+5)(2l+7)(2l+9)}.$$

All other coefficients vanish due to selection rules on the quantum number l. Besides this, we note that the coefficient matrices are symmetric $C_{ll'}^{(j)} = C_{l'l}^{(j)}$.

In Fig. 12 we show the spectrum for the parameters $\phi = \pi/4$, $\omega_\perp = 2\pi \times 4.5$ kHz, and $\omega_a = 2\pi \times 1.8$ kHz, which is the same axial trapping frequency as used in Fig. 2. We note that for such calculation we have obtained a set of 1838 eigenfunctions and energies including bound states as well as

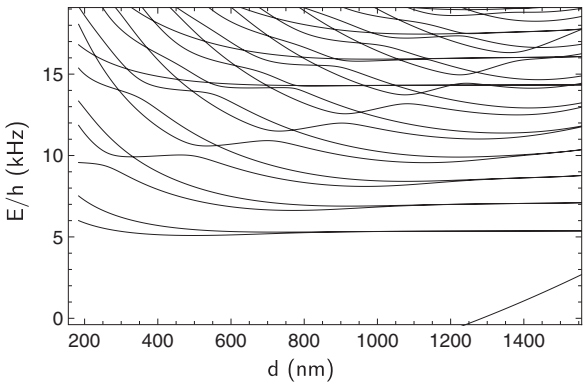

FIG. 12. Three-dimensional eigenenergy spectrum as a function of interwell separation d for a ^{87}Rb atom and a pinned $^{171}Yb^+$ ion assuming a 3D short-range phase of $\phi = \pi/4$, $\omega_a = 2\pi \times 1.8$ kHz, and $\omega_\perp = 2\pi \times 4.5$ kHz.

trap states [10,13]. Apart from the extra angular integration, the whole procedure is very similar to the one used in the 1D calculation and the resulting energy spectrum indeed looks very similar. There are, however, several differences. First, since there are more degrees of freedom, more levels appear. Note also that not all levels are plotted since we limited our discussion to $m = 0$. Second, the exact way in which the energy levels split close to the ion is different. This behavior, however, is related to the choice of the short-range phase. To determine the exact form experimental input would be needed in the form of a scattering length.

APPENDIX B: MICROMOTION HAMILTONIAN

Following Refs. [32,42], we start by writing the ion wave function as

$$\Psi(z_i,t) = \exp\left(-\frac{i}{4\hbar} m_i q \Omega z_i^2 \sin(\Omega t)\right) w(z_i,t). \tag{B1}$$

By substituting this function in Eq. (15) the following effective Hamiltonian for the wave function $w(z_i,t)$ is obtained:

$$H_{\text{eff}}(t) = \frac{p_i^2}{2m_i} + \frac{1}{2} m_i \omega_i^2 z_i^2 + H_{mm}(t), \tag{B2}$$

with the micromotion term given by

$$H_{mm}(t) = -m_i g^2 \omega_i^2 z_i^2 \cos(2\Omega t) - g\omega_i \{z_i, p_i\} \sin(\Omega t). \tag{B3}$$

The secular trapping frequency is given by

$$\omega_i = \frac{\Omega}{2}\sqrt{a + \frac{q^2}{2}}. \tag{B4}$$

In order to evaluate the matrix elements of $H_{mm}(t)$, that is, Eqs. (19) and (20), it is very useful to note that $\langle \psi_{l'}^{(d)} | \{p,r\} | \psi_l^{(d)} \rangle = i\mu \langle \psi_{l'}^{(d)} | [H^{(d)}, r^2] | \psi_l^{(d)} \rangle / \hbar$. Similarly, $\langle \psi_{l'}^{(d)} | p | \psi_l^{(d)} \rangle = i\mu \langle \psi_{l'}^{(d)} | [H^{(d)}, r] | \psi_l^{(d)} \rangle / \hbar$ [32]. Equivalent equations hold for the center-of-mass coordinate too.

[1] A. T. Grier, M. Cetina, F. Oručević, and V. Vuletić, Phys. Rev. Lett. **102**, 223201 (2009).
[2] C. Zipkes, S. Paltzer, C. Sias, and M. Köhl, Nature (London) **464**, 388 (2010).
[3] S. Schmid, A. Härter, and J. H. Denschlag, Phys. Rev. Lett. **105**, 133202 (2010).
[4] C. Zipkes, S. Palzer, L. Ratschbacher, C. Sias, and M. Köhl, Phys. Rev. Lett. **105**, 133201 (2010).
[5] A. Härter and J. H. Denschlag, Contemp. Phys. **55**, 33 (2014).
[6] M. Krych, W. Skomorowski, F. Pawłowski, R. Moszynski, and Z. Idziaszek, Phys. Rev. A **83**, 032723 (2011).
[7] W. G. Rellergert, S. T. Sullivan, S. Kotochigova, A. Petrov, K. Chen, S. J. Schowalter, and E. R. Hudson, Phys. Rev. Lett. **107**, 243201 (2011).
[8] C. Kollath, M. Köhl, and T. Giamarchi, Phys. Rev. A **76**, 063602 (2007).
[9] J. Goold, H. Doerk, Z. Idziaszek, T. Calarco, and T. Busch, Phys. Rev. A **81**, 041601(R) (2010).
[10] H. Doerk, Z. Idziaszek, and T. Calarco, Phys. Rev. A **81**, 012708 (2010).
[11] T. Calarco, U. Dorner, P. Julienne, C. Williams, and P. Zoller, Phys. Rev. A **70**, 012306 (2004).
[12] M. Krych and Z. Idziaszek, Phys. Rev. A **80**, 022710 (2009).
[13] R. Gerritsma, A. Negretti, H. Doerk, Z. Idziaszek, T. Calarco, and F. Schmidt-Kaler, Phys. Rev. Lett. **109**, 080402 (2012).
[14] M. Albiez, R. Gati, J. Fölling, S. Hunsmann, M. Cristiani, and M. K. Oberthaler, Phys. Rev. Lett. **95**, 010402 (2005).
[15] I. Bausmerth, U. R. Fischer, and A. Posazhennikova, Phys. Rev. A **75**, 053605 (2007).
[16] U. R. Fischer, C. Iniotakis, and A. Posazhennikova, Phys. Rev. A **77**, 031602(R) (2008).
[17] R. Gati and M. K. Oberthaler, J. Phys. B **40**, R61 (2007).
[18] S. Levy, E. Lahoud, I. Shomroni, and J. Steinhauer, Nature (London) **449**, 579 (2007).
[19] L. J. LeBlanc, A. B. Bardon, J. McKeever, M. H. T. Extavour, D. Jervis, J. H. Thywissen, F. Piazza, and A. Smerzi, Phys. Rev. Lett. **106**, 025302 (2011).
[20] I. Bouchoule, Eur. Phys. J. D **35**, 147 (2005).
[21] T. Betz *et al.*, Phys. Rev. Lett. **106**, 020407 (2011).
[22] A. Eckardt, T. Jinasundera, C. Weiss, and M. Holthaus, Phys. Rev. Lett. **95**, 200401 (2005).
[23] J. Grond *et al.*, New J. Phys. **13**, 065026 (2011).
[24] N. Bar-Gill, C. Gross, I. Mazets, M. Oberthaler, and G. Kurizki, Phys. Rev. Lett. **106**, 120404 (2011).
[25] Q. Y. He, M. D. Reid, T. G. Vaughan, C. Gross, M. Oberthaler, and P. D. Drummond, Phys. Rev. Lett. **106**, 120405 (2011).
[26] U. Bissbort, D. Cocks, A. Negretti, Z. Idziaszek, T. Calarco, F. Schmidt-Kaler, W. Hofstetter, and R. Gerritsma, Phys. Rev. Lett. **111**, 080501 (2013).
[27] I. Bloch, J. Dalibard, and S. Nascimbène, Nat. Phys. **8**, 267 (2012).
[28] R. Blatt and C. F. Roos, Nat. Phys. **8**, 277 (2012).
[29] Z. Lan and C. Lobo, arXiv:1310.4152.
[30] Z. Idziaszek, T. Calarco, and P. Zoller, Phys. Rev. A **76**, 033409 (2007).
[31] Z. Idziaszek, A. Simoni, T. Calarco, and P. S. Julienne, New J. Phys. **13**, 083005 (2011).
[32] L. H. Nguyên, A. Kalev, M. Barrett, and B.-G. Englert, Phys. Rev. A **85**, 052718 (2012).
[33] M. Cetina, A. T. Grier, and V. Vuletić, Phys. Rev. Lett. **109**, 253201 (2012).
[34] M. Krych and Z. Idziaszek, arXiv:1312.0279.
[35] D. A. Steck, http://steck.us/alkalidata/.
[36] A. Miffre *et al.*, Eur. Phys. J. D **38**, 353 (2005).
[37] B. R. Johnson, J. Chem. Phys. **67**, 4086 (1977).
[38] G. J. Milburn, J. Corney, E. M. Wright, and D. F. Walls, Phys. Rev. A **55**, 4318 (1997).
[39] D. Leibfried, D. M. Meekhof, B. E. King, C. Monroe, W. M. Itano, and D. J. Wineland, Phys. Rev. Lett. **77**, 4281 (1996).
[40] F. Ziesel *et al.*, J. Phys. B **46**, 104008 (2013).
[41] T. Caneva, T. Calarco, and S. Montangero, Phys. Rev. A **84**, 022326 (2011).
[42] R. J. Cook, D. G. Shankland, and A. L. Wells, Phys. Rev. A **31**, 564 (1985).
[43] C. Schneider, M. Enderlein, T. Huber, and T. Schaetz, Nat. Photon. **4**, 772 (2010).

[44] M. Enderlein, T. Huber, C. Schneider, and T. Schaetz, Phys. Rev. Lett. **109**, 233004 (2012).
[45] *Atom Chips*, edited by J. Reichel and V. Vuletić (Wiley-VCH, Weinheim, 2011).
[46] J. Reichel, W. Hänsel, and T. W. Hänsch, Phys. Rev. Lett. **83**, 3398 (1999).
[47] H. Ott, J. Fortagh, G. Schlotterbeck, A. Grossmann, and C. Zimmermann, Phys. Rev. Lett. **87**, 230401 (2001).
[48] R. Folman *et al.*, Adv. At. Mol. Opt. Phys. **48**, 263 (2002).
[49] S. Seidelin *et al.*, Phys. Rev. Lett. **96**, 253003 (2006).
[50] J. I. Cirac and P. Zoller, Nature (London) **404**, 579 (2000).
[51] D. Kielpinski, C. Monroe, and D. J. Wineland, Nature (London) **417**, (2002).
[52] F. Mintert and C. Wunderlich, Phys. Rev. Lett. **87**, 257904 (2001).
[53] D. Leibfried, E. Knill, C. Ospelkaus, and D. J. Wineland, Phys. Rev. A **76**, 032324 (2007).
[54] C. Ospelkaus *et al.*, Nature (London) **476**, 181 (2011).
[55] S. X. Wang *et al.*, Appl. Phys. Lett. **94**, 094103 (2009).
[56] J. Welzel *et al.*, Eur. Phys. J. D **65**, 285 (2011).
[57] J. Joger, Master's thesis, Johannes Gutenberg Universität Mainz, 2013, available at www.hyqs.uni-mainz.de.
[58] R. Gerritsma *et al.*, Nature (London) **463**, 68 (2010).